PCCP

PAPER

View Article Online
View Journal | View Issue

Cite this: *Phys. Chem. Chem. Phys.*, 2022, **24**, 27212

Q-Band relaxation in chlorophyll: new insights from multireference quantum dynamics†

Sebastian Reiter, ‡[a] Lena Bäuml,‡[a] Jürgen Hauer [b] and Regina de Vivie-Riedle *[a]

The ultrafast relaxation within the Q-bands of chlorophyll plays a crucial role in photosynthetic light-harvesting. Yet, despite being the focus of many experimental and theoretical studies, it is still not fully understood. In this paper we look at the relaxation process from the perspective of non-adiabatic wave packet dynamics. For this purpose, we identify vibrational degrees of freedom which contribute most to the non-adiabatic coupling. Using a selection of normal modes, we construct four reduced-dimensional coordinate spaces and investigate the wave packet dynamics on XMS-CASPT2 potential energy surfaces. In this context, we discuss the associated computational challenges, as many quantum chemical methods overestimate the Q_x–Q_y energy gap. Our results show that the Q_x and Q_y potential energy surfaces do not cross in an energetically accessible region of the vibrational space. Instead, non-adiabatic coupling facilitates ultrafast population transfer across the potential energy surface. Moreover, we can identify the excited vibrational eigenstates that take part in the relaxation process. We conclude that the Q-band system of chlorophyll *a* should be viewed as a strongly coupled system, where population is easily transferred between the *x* and *y*-polarized electronic states. This suggests that both orientations may contribute to the electron transfer in the reaction center of photosynthetic light-harvesting systems.

Received 27th June 2022,
Accepted 20th September 2022

DOI: 10.1039/d2cp02914f

rsc.li/pccp

1 Introduction

Chlorophylls are a group of natural pigments that play a vital role in photosynthetic light-harvesting.[1–3] There is a variety of differently substituted chlorophylls[4] but in general, the absorption spectrum is dominated by two main bands in the visible range, labeled B- and Q-bands. While the B or Soret band appears as a strong absorption around 400 nm, the weaker Q band resides in the red part of the spectrum around 700 nm and exhibits an extensive pattern of vibrational side bands.

Underlying both absorption bands are four excited states, labeled Q_x/Q_y and B_x/B_y, according to the polarization of the transition dipole moment vector (Fig. 1). These states have historically been characterized with the Gouterman model[6,7] in terms of independent electronic transitions between the four frontier orbitals. In this context, Q_y and B_y are both characterized mainly by the HOMO → LUMO and HOMO−1 → LUMO+1 excitations, albeit with different weights. Similarly, Q_x and B_x are comprised mainly of the HOMO−1 → LUMO and HOMO → LUMO+1 excitations. However, this simplistic model does not explain the ultrafast internal conversion within the Q-bands,[8–11]

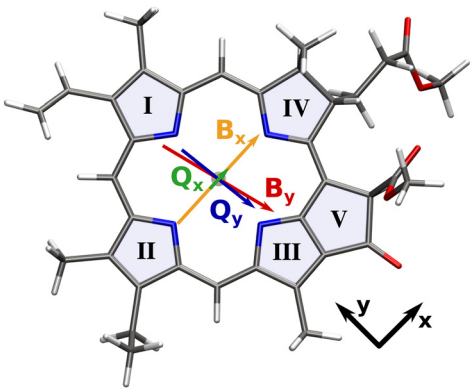

Fig. 1 Transition dipole moments of the Q and B bands overlaid on the molecular structure of our chlorophyll model system. Arrows are scaled with the length of the respective transition dipole vector. Roman numerals signify the ring numbering convention used in this work.[5]

[a] *Department of Chemistry, Ludwig-Maximilians-Universität München, Butenandtstr. 11, 81377 Munich, Germany. E-mail: regina.de_vivie@cup.uni-muenchen.de*
[b] *Department of Chemistry, Technical University of Munich, Lichtenbergstr. 4, 85747 Garching, Germany*

† Electronic supplementary information (ESI) available: Details on the chosen methods with sample OpenMolcas input, optimized geometries and coordinate vectors, potential energy surfaces, non-adiabatic coupling matrix elements, transition dipole moments and additional quantum dynamics simulations. See DOI: https://doi.org/10.1039/d2cp02914f

‡ These authors contributed equally to this work.

which plays an important role in energy and exciton transfer during photosynthetic light-harvesting.[12] In particular, magnetic circular dichroism (MCD) and polarized fluorescence spectra of chlorophyll *a* exhibit not just one but two *x*-polarized bands, whose energetic positions are also strongly dependent on the solvent.[8,13–16] Relative to the Q_y 0–0 band maximum, the lower-energy component appears at 700 cm^{-1} (1100 cm^{-1}) in diethyl-ether (pyridine), while the higher-energy band occurs at 1700 cm^{-1} (2100 cm^{-1}). Their assignment to an electronic state has been the subject of debate for several decades. The ''traditional'' assignment[15,17] identifies the higher energy band as the Q_x origin, while the ''modern'' assignment[16,18] favors the lower energy component. Adding to the confusion, the historical assignment of the Q_x state to the lower- or higher-energy band also changes with the solvent coordination pattern of the central magnesium ion.[19] A recent re-evaluation of existing experiments in combination with vibronic coupling models[8] indicated that the two transitions are better thought of as a single system of inseparably mixed vibronic states. The strong vibronic coupling between Q_x and Q_y spreads *x*-polarization across the whole Q band system and allows ultrafast population transfer on a timescale of 100 fs to 226 fs, depending on the solvent.[8,20,21]

Here, high-level quantum mechanical calculations can complement experimental findings.[8,22–24] In particular, non-adiabatic dynamics simulations can shed light on the mechanism behind the strong vibronic coupling. Most studies employ a semiclassical ansatz, where the internal molecular dynamics are modeled as point masses moving in a quantum mechanical electrostatic potential.[9–11,25] While this approach is able to capture the molecular dynamics in full dimensionality, it is inherently limited by the need to calculate energy gradients in every time step for many trajectories with simulation times up to several picoseconds. These requirements limit the level of theory, as most multireference methods quickly become prohibitively expensive if gradients are involved. Moreover, a classical treatment of nuclear motion neglects the coherence of the wave packets in strongly coupled potentials as well as the interaction with the laser field.

In this paper, we therefore investigate the ultrafast relaxation within the Q-bands of a chlorophyll *a* analogue through the lens of wave packet quantum dynamics in reduced dimensionality. We first evaluate a variety of quantum chemical methods for their ability to adequately describe both states in question. Next, we present multiple two-dimensional coordinate spaces to construct XMS-CASPT2 potential energy surfaces (PESs), on which we model the ultrafast population transfer. We discuss the topography of the excited state potentials and its implications on the wave packet dynamics. In particular, we show how population can be transferred not only from the energetically higher Q_x state to the lower Q_y state, but also the other way round after laser excitation into vibrational side bands of Q_y. Finally, the results are complemented by a simulation of the coupled nuclear and electron dynamics within the Q-band, using the NEMol ansatz.[26–30] Our results shed light on the intimate coupling of the two Q states in chlorophyll and provide a reference for future theoretical and experimental studies.

2 Methods

All calculations in this work use a reduced model of chlorophyll *a*, where the phytyl chain is replaced by a methyl group. This reduces the number of atoms from 137 to 82 and speeds up the calculations at negligible errors in the absorption energies, which has been shown before[5,31] and was validated again by us (Fig. S1, ESI†).

Molecular visualizations within this work were created with VMD 1.9.3.[32,33] Orbitals for CASSCF/-PT2 calculations were visualized with Luscus 0.8.6.[34]

2.1 Geometry optimizations

The ground state geometry of our chlorophyll model was optimized with the CAM-B3LYP density functional[35] and the 6-311G(d) basis set[36–38] using Gaussian 16.[39] The Q_y and Q_x states were optimized with the same functional and basis set at the TDDFT level. Optimized geometries were verified as energy minima by the absence of imaginary vibrational frequencies.

2.2 Excited state calculations

We tested a range of density functionals, namely CAM-B3LYP,[35] ωB97X-D,[40] ωB97X-D4,[41] BHLYP,[42,43] LC-ωHPBE[44] and M062X[45] to calculate chlorophyll excitation energies with a special focus on the Q_x–Q_y energy gap. These test calculations were conducted with Gaussian 16 and the 6-311G(d) basis set,[36–38] with the exception of ωB97X-D4,[41] which is implemented in Orca 5.0[46–48] and where the def2-TZVP basis[49] was employed.

While some of the density functionals gave promising results for the position of the Q-bands at the Franck–Condon (FC) geometry, investigating the ultrafast non-adiabatic population transfer requires the use of a multireference method. Therefore, we used the DFT/MRCI method[50–52] with the redesigned R2018 Hamiltonian[53] as a benchmark reference for all other methods. The Kohn–Sham reference orbitals were calculated at the BHLYP[42,43]/def2-SV(P)[49] level of theory using the resolution of the identity approximation for Coulomb and exchange integrals[54,55] (RI-JK) with the def2-SVP/C[56] and def2/JK[57] auxiliary basis sets, as implemented in Orca 4.2.[46,47] An MRCI reference space was constructed iteratively for 50 roots, starting from a CISD expansion of four electrons in the four frontier orbitals, until the leading configurations of all roots were contained in the reference space. In the DFT/MRCI formalism, a parametrized damping function is applied to the MRCI matrix elements. This is done to avoid double counting of dynamic electron correlation, which has already been accounted for by the DFT part, and brings along an energy-based selection of configurations.[52,53] In this work, we have used the short selection threshold of 0.8 E_h with the corresponding parameter set. The short MRCI expansion speeds up the calculations considerably, while providing an excellent absorption spectrum for our chlorophyll analogue.

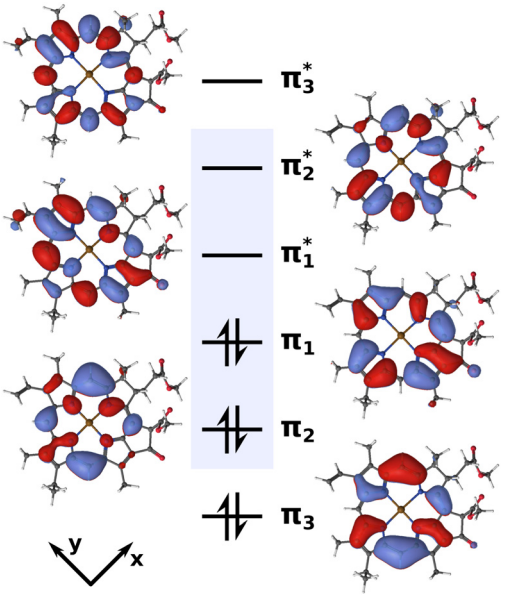

Fig. 2 Active space of six electrons in six orbitals (isovalue 0.02) used for the XMS-CASPT2 calculations. The blue box highlights the four Gouterman orbitals.

CASSCF[58] and (X)MS-CASPT2[59–64] calculations were conducted with OpenMolcas 19.11[65,66] using the ANO-RCC-VDZP[67–69] basis set. Great care must be taken in the selection of active spaces for multi-configurational approaches. Previous theoretical investigations have achieved reasonable results with small,[70] medium-sized[71,72] and very large[22,23] active spaces. After initial testing, we settled on an active space of six electrons in six orbitals (Fig. 2) to construct a PES, as we will detail later.

A balanced description of both Q_y and Q_x was achieved by state-averaging over six roots (SA6) in the CASSCF wave function and allowing all of them to mix in the subsequent XMS-CASPT2 calculation. Using both an IPEA and imaginary shift of 0.1, we obtained a Q_x–Q_y energy gap of 0.21 eV at the FC point, which matched the one calculated with DFT/MRCI (0.23 eV) almost exactly. However, this strategy turned out to be problematic for computing a PES. The higher excited states would cause rotations between active and inactive orbitals at geometries away from the FC region, thus introducing discontinuities in the PES. To mitigate this issue, we reduced the number of roots to four, resulting in an SA4-CASSCF(6,6) reference wave function. Here, the active space remained stable across the PES at the cost of strongly overestimating the Q_x–Q_y energy gap at the FC point with 0.54 eV. To get the best of both worlds, we calculated the CASSCF wave function in two steps. In the first step, the molecular orbitals were optimized in a SA4-CASSCF(6,6) scheme to arrive at a stable active space. In the second step, these orbitals were used in a SA6-CASCI(6,6) calculation where only the CI coefficients were re-optimized. Finally, all six roots were mixed in the subsequent XMS-CASPT2 calculation, using an IPEA[73] and imaginary level shift[74] of 0.1. In this way, we were able to stabilize the active space composition across the PES and still achieve a Q_x–Q_y gap of 0.39 eV, closer to the DFT/MRCI reference than in a pure SA4-XMS-CASPT2(4,4) scheme. Energies for both of the state-averaging schemes with various level shifts, along with an exemplary OpenMolcas input are provided in the ESI.† To account for the remaining deviation of the Q_x–Q_y gap from the DFT/MRCI reference, the calculated Q_x PESs were finally shifted down by −0.16 eV.

2.3 Quantum dynamics

For the wave packet quantum dynamics, the time-dependent Schrödinger equation was solved on a spatial grid of 256 × 256 points, using the Chebyshev[75] propagation scheme in a program of our own design. Energies, transition dipole moments and non-adiabatic coupling matrix elements (NACs) were calculated at 45 grid points (Fig. S5–S11, ESI†) and interpolated to the target grid with thin-plate splines.[76] Since the use of XMS-CASPT2 gradients would have been too expensive, NACs were calculated in the SA4-CASSCF(6,6)/SA6-CASCI(6,6) scheme introduced above. To still account for the correct energy difference between the Q_x and Q_y state, we scaled the NACs with the ratio of the energy gap at the XMS-CASPT2 and the CASSCF level. Furthermore, the full-dimensional NAC vector was projected onto the respective 2D coordinate space. The kinetic energy in the reduced-dimensional coordinate space was expressed in the Wilson G-matrix formalism[77–80] and matrix elements are provided in Table S9, ESI.† Vibrational eigenfunctions of the 2D potentials were calculated by propagation in imaginary time.[81]

2.4 Coupled nuclear and electron dynamics in molecules (NEMol)

The coupled nuclear and electron dynamics was determined using the NEMol ansatz[26–30] developed in our group. Within this purely quantum-mechanical ansatz the electronic wave functions are propagated in the eigenstate basis and coupled to the nuclear wave packet propagated on coupled PESs. In this work a NEMol-grid[29,30] of 45 grid points with the same dimensions and spacing as for the calculations of the energies, transition dipole moments and NACs was used. Using the NEMol ansatz, the coupled one-electron density is determined. Applying the NEMol-grid the integration over the full nuclear coordinate space is split up into segments. Summing up over the partial densities of all of these segments, the total electron density coupled to multiple nuclear grid points is obtained.

3 Results and discussion

3.1 Assessment of quantum-chemical methods

The Q-band relaxation of chlorophyll strongly depends on the energy gap between the Q_x and Q_y state. Any theoretical investigation of the process therefore first requires a method which can adequately model both excited states and ideally also the rest of the observed spectrum. To assess different methods in this regard, we computed steady-state absorption spectra and compared them against an experimental spectrum[82,83] for chlorophyll *a* measured in diethyl ether (Fig. 3a)).

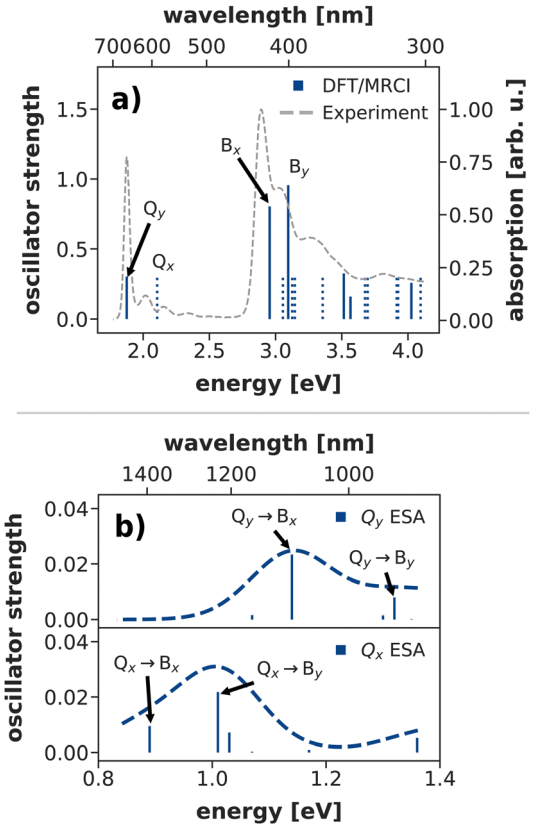

Fig. 3 (a) Calculated steady state absorption spectrum of a chlorophyll model system at the DFT/MRCI level of theory, compared to an experimental spectrum of chlorophyll *a* in diethyl ether.[82,83] The depicted absorption lines are red-shifted by 0.11 eV to the position of the experimental Q_y band. (b) Excited state absorption spectra from the Q-bands at the DFT/MRCI level of theory (unshifted).

We shall start our comparison with the DFT/MRCI method. Here, we only observe a small systematic blue-shift of the entire spectrum by 0.11 eV. The calculated absorption lines coincide well with the experimental band shape, even though the blue-shift is slightly stronger in the B bands. Both Q_y and Q_x exhibit a significant double excitation character of 9% and 12%, respectively. The contribution from double excitations only increases in the B band with 14% for B_x and 18% for B_y, highlighting the need for a multireference method. In contrast to earlier DFT/MRCI calculations,[84] which report an additional doubly excited state in the visible region, we observe B_x as the third excited state. However, a dark state with 19% double-excitation character occurs at 392 nm, between B_x and B_y in our calculations. The difference may be due to our use of the revised R2018 DFT/MRCI Hamiltonian[52] as well as a different optimized geometry.

To further assess the quality of DFT/MRCI for chlorophyll excitations, we computed transient spectra from both the Q_x and Q_y bands (Fig. 3b)). An experimental spectrum is available for a peridinin–chlorophyll-protein complex.[85] After 0.5 ps, when all initial population in Q_x should have decayed, it features an excited state absorption around 1290 nm which is consequently assigned to a series of transitions from Q_y to energetically higher states.[85] In comparison, the Q_y absorption predicted by DFT/MRCI occurs at lower wavelengths around 1100 nm. The difference is in part due to the overestimation of the B–Q energy gap by DFT/MRCI, and partly due to protein–chlorophyll interactions that may shift the excited state absorption in the experiment.

Overall, the DFT/MRCI method is in excellent agreement with the experimental absorption spectrum and, most importantly, it provides a balanced description of the major absorption bands. From this we conclude that the position of the Q_x band and thereby the Q_x–Q_y energy gap is correctly reproduced by DFT/MRCI. Therefore, we have used this method as a theoretical benchmark for all other methods in this work.

Apart from DFT/MRCI we also tested different density functionals and active space methods. The resulting vertical excitation energies are reported in Table 1. For the comparison of the different methods we mainly focused on the Q_x–Q_y energy gap, as this is the main parameter that determines the coupling between the two electronic states. In general, TDDFT considerably blue-shifts all vertical excitation energies, which has been observed before[24] and is a result of neglecting double excitations. Consequently, the error increases with higher excited states, where the doubles' contributions become more important. All tested functionals apart from M062X are range-separated but the range-separation does not seem to be crucial for chlorophyll, as M062X stands out as one of the best functionals to describe the Q_x–Q_y gap at the TDDFT level. The consideration of London dispersion forces as in ωB97X-D and its more recent analogue ωB97X-D4 also does not lead to an improvement in accuracy and even further increases the Q_x–Q_y gap. Out of the tested functionals, M062X and CAM-B3LYP (Fig. 3) agree best with the DFT/MRCI results and experimental band assignments. However, all functionals significantly overestimate the Q_x–Q_y gap, which may be a problem for simulating the Q-band dynamics of chlorophyll at the TDDFT level.

Even though DFT/MRCI provides excellent results in this regard, we did not use it to compute PESs modeling the Q-band dynamics, as it does not provide the gradients needed to construct the NAC between the two states. As an alternative, we investigated the CASSCF and (X)MS-CASPT2 methods. We compared the size and composition of the active space as well as the type and magnitude of applied level shifts with the goal to reproduce the Q_x–Q_y gap at a small enough computational cost to calculate PESs. In particular, we investigated four active spaces of different sizes. The smallest AS(6,6) contained the four Gouterman orbitals and a further pair of π/π*-orbitals, amounting to six electrons in six molecular orbitals (Fig. 2). The larger spaces AS(8,8) and AS(10,10) respectively contained one or two additional pairs of π/π*-orbitals (Fig. S2 and S3, ESI†) The largest space we tested featured 22 electrons in 22 orbitals in a restricted active space (RAS) scheme, with the four Gouterman orbitals in the RAS2 subspace, and nine π/π* orbitals each in the RAS1 and RAS3 subspaces (Fig. S4, ESI†). Excitations from RAS1 and into RAS3 were restricted to singles or doubles respectively, while all excitations were allowed within RAS2. All active space based approaches overestimate the experimentally

Table 1 Vertical excitation energies (in eV) of chlorophyll a model system calculated at various levels of theory. The prefix SA*n* refers to state-averaging over *n* states in the CASSCF calculations

	Q_y	Q_x	$\lvert Q_x–Q_y\rvert$	B_x	B_y
CAM-B3LYP	2.17	2.56	0.39	3.48	3.74
wB97X-D	2.09	2.71	0.62	3.58	3.92
wB97X-D4	2.03	2.67	0.64	3.51	3.87
BHandHLYP	2.21	2.61	0.40	3.55	3.83
LC-wHPBE	2.06	2.79	0.73	3.61	3.97
M062X	2.21	2.59	0.38	3.48	3.72
DFT/MRCI	1.99	2.22	0.23	3.07	3.21
SA4-XMS-CASPT2(6,6)[a]	2.28	2.82	0.54	—	—
SA6-XMS-CASPT2(6,6)[b]	2.19	2.40	0.21	3.51	4.15
SA6-XMS-CASPT2(6,6)[a]	2.67	2.98	0.31	4.14	4.82
SA6-XMS-CASPT2(8,8)[a]	2.64	3.17	0.53	4.28	4.40
SA6-XMS-CASPT2(10,10)[a]	2.64	3.04	0.40	4.06	4.36
SA6-MS-RASPT2(22,1,1;9,4,9)[a]	2.34	2.74	0.40	3.39	4.00
SA6-MS-RASPT2(22,2,2;9,4,9)[a]	2.34	2.75	0.41	3.51	3.99
SA4-/SA6-XMS-CASPT2(6,6)[bc]	2.28	2.67	0.39	3.67	4.35
Exp. (“modern”)	1.85[d]/1.88[e]	1.94[d]/2.00[e]	0.09[d]/0.12[e]	—	—
Exp. (“traditional”)	1.88[f]	2.16[f]	0.28[f]	2.90	2.90

[a] IPEA shift: 0.25, imaginary shift: 0.1. [b] IPEA shift: 0.1, imaginary shift: 0.1. [c] SA4-CASSCF/SA6-CASCI/XMS-CASPT2(6,6). [d] “modern” assignment in pyridine.[16,19] [e] “modern” assignment in diethyl ether.[16] [f] “traditional“ assignment in diethyl ether.[15,17,19]

determined excitation energies. While the Q_y state is systematically stabilized when increasing the size of the active space, the Q_x state and consequently the Q_y–Q_x energy gap do not follow this trend. Instead, adding orbitals to the active space favors one state over the other, depending on whether the additional orbitals are oriented more along the *x* or *y* molecular axis. The same behavior is observed for the B_x and B_y states. It is reminiscent of the L_a/L_b states in pyrene, which are also characterized by orthogonally polarized transitions and where a minimal active space proved beneficial for a balanced description of both states.[86] This again highlights the fact that choosing an active space should not rely solely on size criteria.[87,88] In light of these findings, we chose the small AS(6,6) for all further calculations to achieve a Q_y–Q_x energy gap that is close to the DFT/MRCI results at a reasonable computational cost. To keep this active space stable, also for geometries away from the FC region, we finally opted for a consecutive SA4-CASSCF/SA6-CASCI/XMS-CASPT2(6,6) scheme as outlined in the methods section.

Apart from the size and composition of the active space, the use of level shifts can strongly affect the results of CASPT2 calculations. Level shifts, particularly the IPEA[73] and imaginary shift[74] techniques, are a common way to remove intruder states. Indeed, using no level shift at all in the XMS-CASPT2(6,6) calculations introduces a spurious excitation from π_3 to π_1^* as the first excited state. Therefore, we tested various combinations of IPEA and imaginary shifts to alleviate this issue (Tables S3–S6, ESI†). Applying any shift removes the intruder state, but the Q_x–Q_y gap is very sensitive to the exact combination of the two shift values. As the use of the IPEA shift is controversial,[89–92] in particular for porphyrin-based systems,[90,93] we tested applying only an imaginary shift. However, depending on the initial guess for the CASSCF reference, this leads to root-flipping at the FC point, such that Q_y becomes the higher and Q_x the lower energy excited state (Table S3, ESI†). Adding an IPEA shift helped resolve this issue and we therefore regard its use as justified in this case to preserve the correct state-ordering. In the end, combining an IPEA and imaginary shift of 0.1 emerged as a good choice to remove intruder states, ensure the correct state ordering across the PES and maintain a reasonable Q_x–Q_y gap.

3.2 Potential energy surfaces

Studying the quantum dynamics of the Q-band relaxation in chlorophyll requires not only an adequate method, but also a reduced-dimensional coordinate space, which can capture the essence of the relaxation process. To identify suitable coordinates, we calculated the overlap s_i of the normal modes $\mathbf{q}_i$ (with $i = 1,2,\ldots,3N-6$) in mass-weighted Cartesian coordinates, and the normalized NAC vector $\mathbf{f}$ at the minimum geometry of the lower-energy state Q_y:

$$s_i = \sum_j^{3N} f_j \cdot q_{ij} \quad (1)$$

A similar technique has been used before in the context of semiclassical dynamics.[10] As the normal modes span an orthogonal coordinate space, the squared overlap s_i^2 corresponds to the percentage of non-adiabatic coupling contained in each mode $\left(\sum_i s_i^2 = 1\right)$. A complete list of all normal modes, their respective squared overlap with the NAC vector and their harmonic vibrational frequency can be found in Table S10 in the ESI.† Fig. 4 illustrates the magnitude of s_i^2 in each normal mode. We find that many modes are involved in the coupling but three modes stand out, together accounting for 38% of non-adiabatic coupling. The normal mode with the strongest overlap, mode 195 (s^2 = 15.62%), describes an in-plane vibration of the entire porphyrin scaffold and appears at 1596 cm^{-1}. A 1D potential along this mode (Fig. 5) reveals that the Q_x and Q_y

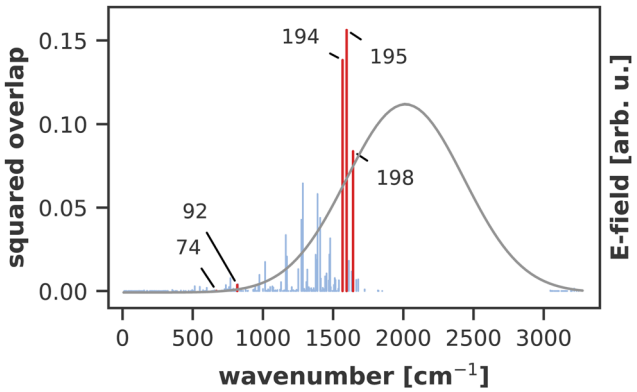

Fig. 4 Squared overlap of each normal mode with the NAC vector at the ground state minimum geometry. Normal modes highlighted in red were used to construct 2D coordinate spaces for the non-adiabatic quantum dynamics. The grey line illustrates the spectral width of the simulated laser pulse. Wavenumbers are given relative to the zero-point energy of Q_y, obtained at the TD-DFT/CAM-B3LYP/6-311G(d) level.

state do not cross in an energetically accessible region of space. Instead, the two potentials run almost parallel to each other, facilitating non-adiabatic coupling across the coordinate space. This is further supported by the fact that the energetic order of the two states, computed at the DFT/MRCI level, is the same at the FC point as at their respective minimum geometries (Table S8, ESI†). So far, a true Q_x/Q_y conical intersection in chlorophyll-like systems has only been identified for free-base porphyrin.[71] Its structure involves displacement of the pyrrolic protons – a coordinate which is not accessible in chlorophylls and other metal–porphyrins.

The normal mode with the second-highest overlap, mode 194 (s^2 = 13.82%) appears at 1568 cm^{-1} and describes a similar collective in-plane vibration as mode 195. Given the strong coupling along these two modes, we used them to construct a 2D coordinate space for non-adiabatic quantum dynamics. To justify this choice of coordinates and to check whether our results also hold up in different coordinate spaces, we also tested three other 2D coordinate spaces between mode 195 and

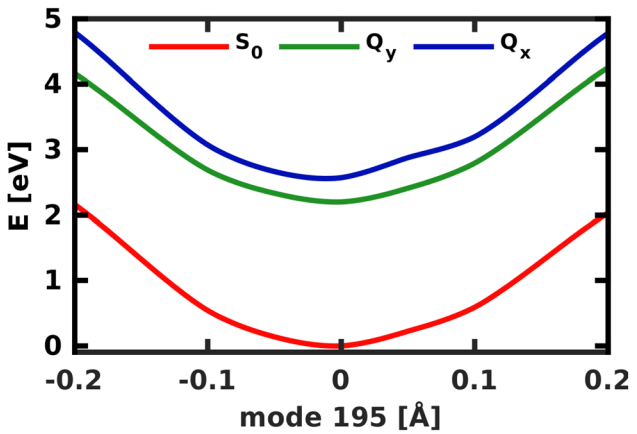

Fig. 5 1D electronic potentials along normal mode 195. Q_x and Q_y do not cross but run almost parallel to each other.

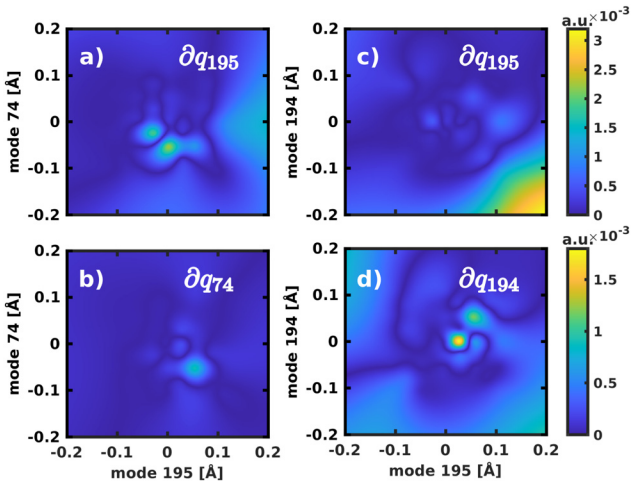

Fig. 6 Visualization of the NACs, projected into the 2D spaces spanned by normal modes 195/74 and 195/194, respectively. The notation ∂q_i refers to the projection of the NACs onto the respective normal mode to yield $\left\langle \Psi_1 \left| \frac{\partial}{\partial q_i} \right| \Psi_2 \right\rangle$.

less strongly coupled modes from different spectral regions, namely modes 198 (s^2 = 8.37%), 92 (s^2 = 0.36%) and 74 (s^2 = 0.005%).

For the 2D spaces spanned by modes 195/194 and 195/74 the NACs are visualized in Fig. 6 respectively to illustrate the extreme cases of strong and weak coupling. The weaker coupling in mode 74 is especially visible when comparing the projection of the NACs onto the respective second normal mode in Fig. 6b and d. However, in all tested coordinate spaces the non-adiabatic coupling is larger than zero across the PES, not localized at singular geometries as would be typical for a conical intersection.

3.3 Non-adiabatic quantum dynamics

To model the non-adiabatic dynamics within the Q-bands, we simulated the evolution of a nuclear wave packet in all four 2D coordinate spaces. For the following analysis, the excited state wave packet was prepared by placing the ground state vibrational eigenfunction of the S_0 potential on the Q_x surface. As we do not simulate coupling to environmental modes or decoherence effects, which take over at long time scales, we will restrict our analysis to the first 150 fs of the dynamics. The temporal evolution of the population in the two spaces 195/194 and 195/74 is illustrated in Fig. 7.

The difference in the coupling strength is clearly reflected in the time it takes until half the population is transferred from Q_x to Q_y. In the strongly coupled 2D space 195/194, the transfer time is less than 10 fs, while in the weakly coupled space 195/74, it is 60 fs. The other weakly coupled 2D space we tested (195/92) fits into this trend with a transfer time of 25 fs. Only mode 198 appears to be more strongly coupled than the other modes, as indicated by higher NACs across the coordinate space (Fig. S9, ESI†), and yields a transfer time of $<$10 fs, only interrupted by strong back-coupling from Q_x to Q_y. The overall

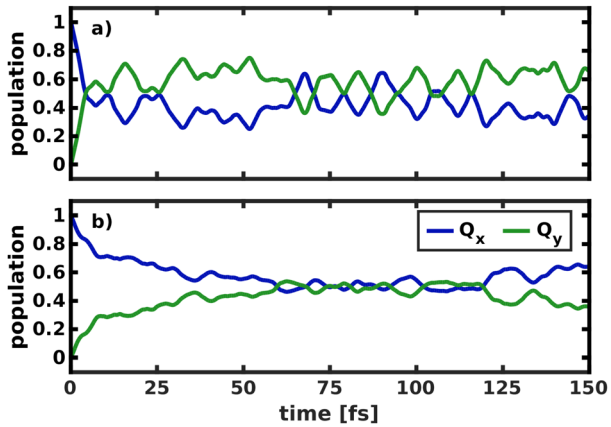

Fig. 7 Population transfer between Q_x and Q_y in the 2D coordinate spaces spanned (a) by normal modes 195/194 and (b) by normal modes 195/74.

trends we observe in the population dynamics are consistent in all tested coordinate spaces and we therefore expect the results to be reliable. After half the population is transferred, back-coupling into Q_x can be observed, as the wave packet cannot dissipate into other nuclear degrees of freedom in the quasi-harmonic 2D space on the Q_y surface. For the same reason, the oscillations caused by this back-coupling do not decay in time. Given that the two potentials run mostly parallel to each other (Fig. 5), it is reasonable to assume a 50/50 population of both states at long time scales, under the assumption that energy is conserved within the Q-band system. If dissipation due to environmental coupling was included, the population would eventually decay to the vibrational ground state of Q_y. These population dynamics are fully in line with the conclusions by Reimers *et al.*, who argued that the Q-bands of chlorophyll should be regarded as an inseparably mixed system of two strongly vibronically coupled states.[8]

To simulate the wave packet dynamics after laser excitation, a pump pulse with a central frequency ω_0 of 2.43 eV, a full width at half maximum (FWHM) of 30 fs and a maximum field strength of 4.9×10^{-3} GV cm^{-1} was used to excite the vibronic ground state eigenfunction in the space 195/194. As the zero-point vibrational energy in the 2D ground state potential is 0.19 eV, the energy of the laser pulse is tuned for excitation into the vibrational ground state of Q_x at 2.62 eV. Its spectrum is broad enough to populate all the modes spanning the reduced-dimensional coordinate space (*cf.* grey line in Fig. 4). The temporal evolution of the population and the simulated laser pulse are depicted in Fig. 8.

Initially, the laser was allowed to interact with both electronic states (Fig. 8a), as would be the case in an experiment. The laser pulse starts to transfer population at 20 fs. Most of the population (52%) is initially transferred to Q_y, as its transition dipole moment is significantly larger than that of Q_x. In the first 40 fs of the excitation, fast oscillations at twice the frequency of the laser pulse can be observed in the Q_y population curve, indicating that the intense laser field moves population back and forth between the ground and excited

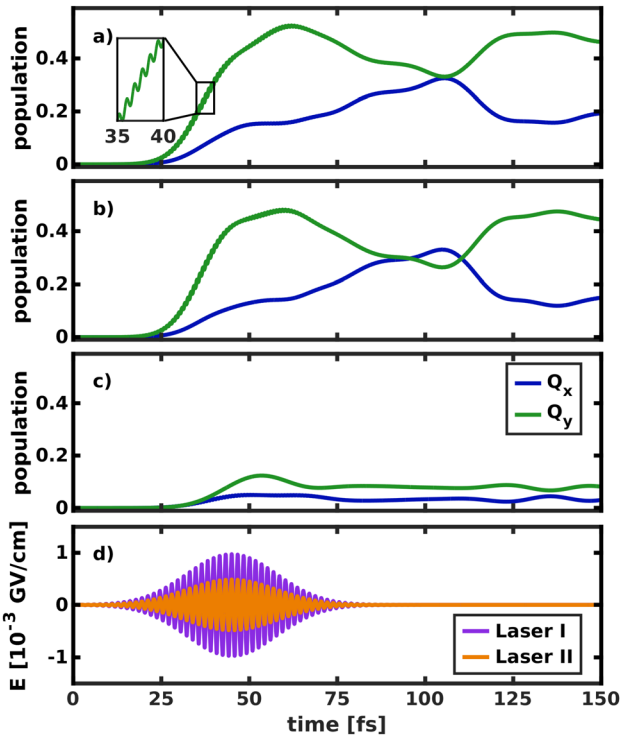

Fig. 8 Temporal evolution of the population in both electronic states after laser excitation into (a) both the Q_y and Q_x state, (b) only the Q_y state and (c) only the Q_x state. (d) Visualization of the simulated laser pulses, where E denotes the electric field strength. The more intense laser I was used only for excitation into the nearly dark Q_x state. The inset in (a) illustrates fast oscillations in the Q_y population, induced by the interaction with the laser field.

state. Immediately after the start of the laser pulse, population is also transferred into Q_x. The population curves in Fig. 8b and c, where only one of the two states can interact with the laser, confirm that most of this population transfer into Q_x does not stem from direct photo-excitation but from the vibronic coupling to Q_y. Conversely, even if the transition dipole moment of Q_y is explicitly turned off (Fig. 8c), such that the laser can only directly excite Q_x, most of the population is instantly transferred into Q_y. This is especially relevant to the assignment of the two experimentally observed absorption bands with *x*-polarization, because it means that even excitation into vibronic side bands of Q_y immediately transfers population to Q_x and *vice versa*. This again corroborates the position that Q_x and Q_y should not be regarded as independent electronic states but rather as a single, strongly coupled system of absorption bands, where *x*- and *y*-polarization is spread across the entire band.

The crossing point where half the population is transferred between the two states occurs at 105 fs, 25 fs after the laser field has decayed. This is around five times as long as in the delta pulse propagation in Fig. 7a and there are also fewer oscillations between the two states. There are two effects that can explain this behavior. First, the laser keeps transferring population into Q_y while the vibronic coupling already populates Q_x, thereby effectively smoothing the fast oscillations visible in Fig. 7a. Second, the laser energy and spectral width are tuned to

match the vibrational ground state of Q_x. In contrast, assuming a delta-pulse by placing an eigenfunction to the S_0 potential on the Q_x surface adds higher-energy components to the excited-state wave packet, which may induce faster oscillations in the population transfer.

To gain deeper insight into the processes after laser excitation, the nuclear wave packet in the Q_y and Q_x electronic potentials is visualized at different points in time in Fig. 9. In the Q_y state (upper panel in Fig. 9), the wave packet exhibits one nodal plane during the laser excitation at 40 fs, barring interferences in regions of stronger vibronic coupling for the moment. It then proceeds to oscillate between two different orientations over time, corresponding to a superposition of the $v = 1$ and $v = 2$ eigenfunctions of the Q_y potential. At 40 fs and 92 fs, the orientation of the wave packet resembles the $v = 2$ vibrational eigenfunction of the Q_y PES, as the energy of this eigenstate matches the central frequency of the laser pulse and is nearly degenerate with the vibronic ground state of Q_x ($v = 0$, Fig. 10). At 72 fs and 105 fs, the wave packet rotates to resemble the $v = 1$ eigenstate of Q_y. The rotations decay over time and stop around 130 fs with a linear combination of the $v = 1$ and $v = 2$ eigenstates of Q_y. On the Q_x surface (bottom panel in Fig. 9), a wave packet corresponding to $v = 0$ appears immediately after laser excitation and increases in amplitude over time due to vibronic coupling to Q_y. The region of stronger coupling around $q_{195} = 0.025$ Å/$q_{194} = 0.025$ Å (*cf.* Fig. 6d)) is clearly reflected in interferences in this part of the PES. Maintaining the coherence between the two electronic states, the Q_x wave packet also rotates along with its counterpart on Q_y. As back-coupling sets in around 50 fs, a second node appears on the Q_y wave packet, corresponding to the current population in Q_x.

3.4 Coupling of nuclear and electronic dynamics

Applying the NEMol ansatz we are able to visualize not only the nuclear but also the coupled nuclear and electron dynamics.

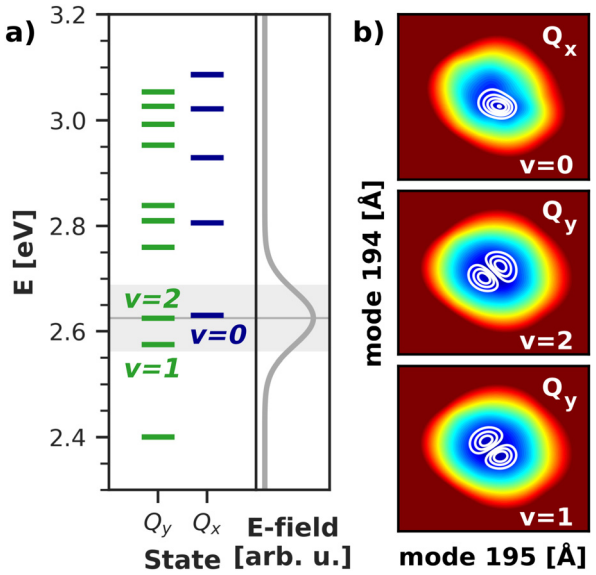

Fig. 10 (a) Vibrational energy levels of the electronic Q_y and Q_x states in a 2D space spanned by normal modes 195/194. The highlighted area illustrates the spectral width (FWHM) of the simulated laser pulse. Energies are given relative to the energy of the electronic ground state. (b) Visualization of the relevant vibrational eigenfunctions in the Q_x and Q_y potentials. Axis ranges and color scheme are identical to those in Fig. 9.

We performed this analysis for the propagation in the 2D space spanned by modes 195/194 by placing the ground state vibrational eigenfunction of the S_0 potential onto the Q_x surface. The corresponding population curve of the nuclear dynamics is shown in Fig. 7. Using the NEMol ansatz it would also be possible to study the excitation pulse induced dynamics, but as we are mainly interested in characterizing the coupling between Q_x and Q_y we have considered only the process after delta pulse excitation. The dipole moment induced by the

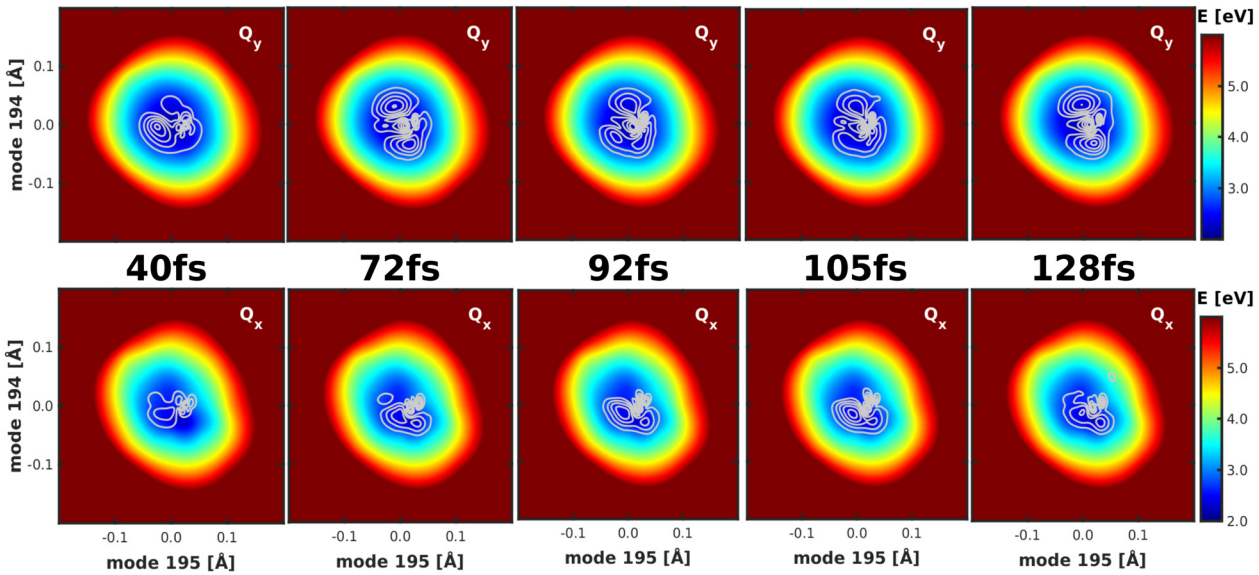

Fig. 9 Visualization of the wave packet after laser excitation into the Q_x state at four different points in time on the Q_y (upper panel) and the Q_x (lower panel) PES spanned by modes 195/194.

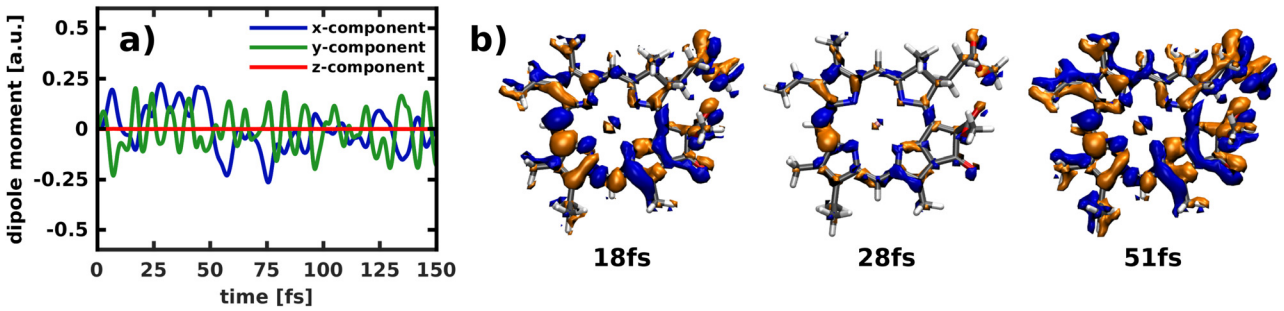

Fig. 11 Temporal evolution of (a) the induced dipole moment obtained by building the difference between a calculation with and without electronic coherence and (b) the difference in density relative to the first frame of the simulation (isovalue: ±0.001). As the propagation starts in the Q_x state, all non-vanishing difference density is indicative for population of the Q_y state. Electron-gain is visualized in blue, electron-loss in orange. These results refer to the propagation after delta pulse excitation depicted in (Fig. 7a).

electronic coherence is depicted in (Fig. 11a). It is calculated by taking the difference between the dipole moment obtained with and without electronic coherence and applying a Fourier transform of the obtained values. There is no dipole moment induced in the *z*-direction, whereas there are fast oscillations visible for both *x*- and *y*-component. They have a similar oscillation period with the ones of the *y*-component being slightly faster. As Q_y is the lower electronic state, the wave packet can couple to more vibrational overtones, which also leads to faster oscillations in the coherence-induced dipole moment.

Another way to visualize the oscillating dynamics between the two states is *via* the electronic difference densities shown in (Fig. 11b). They illustrate the difference between the electronic density at a point in time relative to the first frame of the simulation ($t = 0$). As the propagation starts in the Q_x state, all non-vanishing difference density is indicative for population of the Q_y state. The difference density at 51 fs shows the largest difference as the Q_y states exhibits a maximum in population at this point in time. At 18 fs the Q_y population in (Fig. 7a) exhibits a local maximum, which is also reflected in the difference density. In contrast, the frame at 28 fs shows smaller but still non-negligible differences to the Q_x density, which corresponds well to the nearly equally population of both states at this point in time. The strongest feature in the difference density is the change at the bridging carbon between rings I and II, which is still present when Q_x and Q_y are equally populated. The more population is present in Q_y the more changes also occur throughout the rest of the molecule, as is clearly visible in the snapshot at 51 fs. Using the difference density obtained with the NEMol ansatz therefore allows to visualize the electronic wave packet created due to the non-adiabatic coupling between the first two excited states, taking into account the quantum nature of both nuclear and electronic motion. Its long-lived coherence reaffirms the existence of a strongly coupled Q_x/Q_y system, rather than two independent electronic states.

4 Conclusions

We have simulated the internal conversion dynamics in the Q-bands of chlorophyll, fully taking into account the quantum nature of electronic and nuclear motion. This requires a computational method that reproduces the energy gap between the two excited states. Here, we are faced with the challenge of balancing computational cost with accuracy. Many affordable methods like TD-DFT overestimate the Q_y–Q_x gap, which may adversely affect the simulated coupling between the two states. Our tests once again[24] highlight the need for high-level, ideally multireference methods like DFT/MRCI to capture the effect of higher-order excitations on the spectral features of chlorophylls.

A conical intersection between Q_x and Q_y could not be found as the PESs studied along the selected normal mode coordinates run parallel to each other and the energetic state-ordering is retained upon relaxation in the excited states. Our results instead show the presence of strong vibronic coupling between Q_y and Q_x across the PES in multiple 2D coordinate spaces, due to strongly delocalized non-adiabatic coupling. A simple description of the Q-band system in terms of the Born-Oppenheimer approximation can therefore not be sufficient. In agreement with previous conclusions,[8] but at a higher level of theory and from a different perspective, we conclude that the Q-band of chlorophyll is better thought of as a single system of strongly vibronically coupled states, where *x*-polarization can be spread across the vibronic side bands of Q_y and *vice versa*. Using the NEMol ansatz, we could visualize how the electronic density, coupled to the nuclear motion, oscillates back and forth between *x*- and *y*-polarization. This strong mixing of the electronic states in chlorophyll *a* may have important implications for the charge transport in the reaction center of photosynthetic light-harvesting complexes. After excitation into the higher-energy absorption bands, the population will eventually decay into the Q-bands and from there facilitate electron transfer to neighboring pigments. This process may become more efficient if both *x*- and *y*-polarizations can contribute to it.

Author contributions

Sebastian Reiter: conceptualization, data curation, formal analysis, investigation, methodology, software, validation, visualization, writing – original draft, writing – review & editing; Lena Bäuml: conceptualization, data curation, formal analysis, investigation, methodology, software, validation, visualization,

writing – original draft, writing – review & editing; Jürgen Hauer – funding acquisition, supervision, writing – review & editing; Regina de Vivie-Riedle – conceptualization, funding acquisition, project administration, resources, supervision, writing – review & editing.

Conflicts of interest

There are no conflicts to declare.

Acknowledgements

We thank Eva Sextl for support in the preliminary test calculations. We gratefully acknowledge funding by the Deutsche Forschungsgemeinschaft (DFG, German Research Foundation) through the cluster of excellence e-conversion under Germany's Excellence Strategy – EXC 2089/1 – 390776260.

Notes and references

1 R. E. Blankenship, *Molecular Mechanisms of Photosynthesis*, Wiley, 3rd edn, 2021.
2 A. N. Melkozernov, J. Barber and R. E. Blankenship, *Biochemistry*, 2006, **45**, 331–345.
3 J. R. Reimers, M. Biczysko, D. Bruce, D. F. Coker, T. J. Frankcombe, H. Hashimoto, J. Hauer, R. Jankowiak, T. Kramer, J. Linnanto, F. Mamedov, F. Müh, M. Rätsep, T. Renger, S. Styring, J. Wan, Z. Wang, Z.-Y. Wang-Otomo, Y.-X. Weng, C. Yang, J.-P. Zhang, A. Freiberg and E. Krausz, *Biochim. Biophys. Acta Bioenerg.*, 2016, **1857**, 1627–1640.
4 M. Taniguchi and J. S. Lindsey, *Photochem. Photobiol.*, 2021, **97**, 136–165.
5 D. Sundholm, *Chem. Phys. Lett.*, 2000, **317**, 545–552.
6 M. Gouterman, *J. Mol. Spectrosc.*, 1961, **6**, 138–163.
7 M. Gouterman, G. H. Wagnière and L. C. Snyder, *J. Mol. Spectrosc.*, 1963, **11**, 108–127.
8 J. R. Reimers, Z.-L. Cai, R. Kobayashi, M. Rätsep, A. Freiberg and E. Krausz, *Sci. Rep.*, 2013, **3**, 1–8.
9 W. P. Bricker, P. M. Shenai, A. Ghosh, Z. Liu, M. G. M. Enriquez, P. H. Lambrev, H.-S. Tan, C. S. Lo, S. Tretiak, S. Fernandez-Alberti and Y. Zhao, *Sci. Rep.*, 2015, **5**, 13625.
10 P. M. Shenai, S. Fernandez-Alberti, W. P. Bricker, S. Tretiak and Y. Zhao, *J. Phys. Chem. B*, 2016, **120**, 49–58.
11 M. Fortino, E. Collini, J. Bloino and A. Pedone, *J. Chem. Phys.*, 2021, **154**, 094110.
12 M. Rätsep, J. M. Linnanto and A. Freiberg, *J. Phys. Chem. B*, 2019, **123**, 7149–7156.
13 F. Bär, H. Lang, E. Schnabel and H. Kuhn, *Z. Elektrochem., Ber. Bunsenges. phys. Chem.*, 1961, **65**, 346–354.
14 M. Gouterman and L. Stryer, *J. Chem. Phys.*, 1962, **37**, 2260–2266.
15 C. Weiss, *J. Mol. Spectrosc.*, 1972, **44**, 37–80.
16 M. Umetsu, Z.-Y. Wang, M. Kobayashi and T. Nozawa, *Biochim. Biophys. Acta, Bioenerg.*, 1999, **1410**, 19–31.
17 C. Houssier and K. Sauer, *J. Am. Chem. Soc.*, 1970, **92**, 779–791.
18 R. A. Avarmaa and K. K. Rebane, *Spectrochim. Acta, Part A*, 1985, **41**, 1365–1380.
19 L. L. Shipman, T. M. Cotton, J. R. Norris and J. J. Katz, *J. Am. Chem. Soc.*, 1976, **98**, 8222–8230.
20 Y. Shi, J.-Y. Liu and K.-L. Han, *Chem. Phys. Lett.*, 2005, **410**, 260–263.
21 E. Meneghin, C. Leonardo, A. Volpato, L. Bolzonello and E. Collini, *Sci. Rep.*, 2017, **7**, 11389.
22 A. Anda, T. Hansen and L. De Vico, *J. Chem. Theory Comput.*, 2016, **12**, 1305–1313.
23 A. Anda, T. Hansen and L. De Vico, *J. Phys. Chem. A*, 2019, **123**, 5283–5292.
24 A. Sirohiwal, R. Berraud-Pache, F. Neese, R. Izsák and D. A. Pantazis, *J. Phys. Chem. B*, 2020, **124**, 8761–8771.
25 F. Zheng, S. Fernandez-Alberti, S. Tretiak and Y. Zhao, *J. Phys. Chem. B*, 2017, **121**, 5331–5339.
26 D. Geppert, P. von den Hoff and R. de Vivie-Riedle, *J. Phys. B: At., Mol. Opt. Phys.*, 2008, **41**, 074006.
27 P. von den Hoff, I. Znakovskaya, M. F. Kling and R. de Vivie-Riedle, *Chem. Phys.*, 2009, **366**, 139–147.
28 I. Znakovskaya, P. von den Hoff, S. Zherebtsov, A. Wirth, O. Herrwerth, M. J. J. Vrakking, R. de Vivie-Riedle and M. F. Kling, *Phys. Rev. Lett.*, 2009, **103**, 103002.
29 T. Schnappinger and R. de Vivie-Riedle, *J. Chem. Phys.*, 2021, **154**, 134306.
30 L. Bäuml, T. Schnappinger, M. F. Kling and R. de Vivie-Riedle, *Front. Phys.*, 2021, **9**, 1–12.
31 D. Sundholm, *Chem. Phys. Lett.*, 1999, **302**, 480–484.
32 W. Humphrey, A. Dalke and K. Schulten, *J. Mol. Graphics*, 1996, **14**, 33–38.
33 J. Stone, *An Efficient Library for Parallel Ray Tracing and Animation*, Master's thesis (M.S.), University of Missouri-Rolla, 1998, **https://scholarsmine.mst.edu/masters_theses/1747**.
34 G. Kovačević and V. Veryazov, *J. Cheminf.*, 2015, **7**, 16.
35 T. Yanai, D. P. Tew and N. C. Handy, *Chem. Phys. Lett.*, 2004, **393**, 51–57.
36 A. D. McLean and G. S. Chandler, *J. Chem. Phys.*, 1980, **72**, 5639–5648.
37 R. Krishnan, J. S. Binkley, R. Seeger and J. A. Pople, *J. Chem. Phys.*, 1980, **72**, 650–654.
38 M. M. Francl, W. J. Pietro, W. J. Hehre, J. S. Binkley, M. S. Gordon, D. J. DeFrees and J. A. Pople, *J. Chem. Phys.*, 1982, **77**, 3654–3665.
39 M. J. Frisch, G. W. Trucks, H. B. Schlegel, G. E. Scuseria, M. A. Robb, J. R. Cheeseman, G. Scalmani, V. Barone, G. A. Petersson, H. Nakatsuji, X. Li, M. Caricato, A. V. Marenich, J. Bloino, B. G. Janesko, R. Gomperts, B. Mennucci, H. P. Hratchian, J. V. Ortiz, A. F. Izmaylov, J. L. Sonnenberg, D. Williams-Young, F. Ding, F. Lipparini, F. Egidi, J. Goings, B. Peng, A. Petrone, T. Henderson, D. Ranasinghe, V. G. Zakrzewski, J. Gao, N. Rega, G. Zheng, W. Liang, M. Hada, M. Ehara, K. Toyota, R. Fukuda, J. Hasegawa, M. Ishida, T. Nakajima, Y. Honda,

O. Kitao, H. Nakai, T. Vreven, K. Throssell, J. A. Montgomery Jr., J. E. Peralta, F. Ogliaro, M. J. Bearpark, J. J. Heyd, E. N. Brothers, K. N. Kudin, V. N. Staroverov, T. A. Keith, R. Kobayashi, J. Normand, K. Raghavachari, A. P. Rendell, J. C. Burant, S. S. Iyengar, J. Tomasi, M. Cossi, J. M. Millam, M. Klene, C. Adamo, R. Cammi, J. W. Ochterski, R. L. Martin, K. Morokuma, O. Farkas, J. B. Foresman and D. J. Fox, *Gaussian16, Revision A.03*, Gaussian Inc., Wallingford CT, 2009, **https://www.gaussian.com**.

40 J.-D. Chai and M. Head-Gordon, *Phys. Chem. Chem. Phys.*, 2008, **10**, 6615–6620.

41 A. Najibi and L. Goerigk, *J. Comput. Chem.*, 2020, **41**, 2562–2572.

42 A. D. Becke, *J. Chem. Phys.*, 1993, **98**, 1372–1377.

43 C. Lee, W. Yang and R. G. Parr, *Phys. Rev. B: Condens. Matter Mater. Phys.*, 1988, **37**, 785–789.

44 T. M. Henderson, A. F. Izmaylov, G. Scalmani and G. E. Scuseria, *J. Chem. Phys.*, 2009, **131**, 044108.

45 Y. Zhao and D. G. Truhlar, *Theor. Chem. Acc.*, 2008, **120**, 215–241.

46 F. Neese, *WIREs Comput. Mol. Sci.*, 2012, **2**, 73–78.

47 F. Neese, *WIREs Comput. Mol. Sci.*, 2018, **8**, e1327.

48 F. Neese, *WIREs Comput. Mol. Sci.*, 2022, e1606.

49 F. Weigend and R. Ahlrichs, *Phys. Chem. Chem. Phys.*, 2005, **7**, 3297–3305.

50 S. Grimme and M. Waletzke, *J. Chem. Phys.*, 1999, **111**, 5645–5655.

51 M. Kleinschmidt, C. M. Marian, M. Waletzke and S. Grimme, *J. Chem. Phys.*, 2009, **130**, 044708.

52 C. M. Marian, A. Heil and M. Kleinschmidt, *WIREs Comput. Mol. Sci.*, 2018, **9**, e1394.

53 A. Heil, M. Kleinschmidt and C. M. Marian, *J. Chem. Phys.*, 2018, **149**, 164106.

54 F. Weigend, M. Kattannek and R. Ahlrichs, *J. Chem. Phys.*, 2009, **130**, 164106.

55 S. Kossmann and F. Neese, *Chem. Phys. Lett.*, 2009, **481**, 240–243.

56 A. Hellweg, C. Hättig, S. Höfener and W. Klopper, *Theor. Chem. Acc.*, 2007, **117**, 587–597.

57 F. Weigend, *J. Comput. Chem.*, 2008, **29**, 167–175.

58 B. O. Roos, in *Advances in Chemical Physics*, ed. K. P. Lawley, John Wiley & Sons, Ltd, 1987, pp. 399–445.

59 B. O. Roos, P. Linse, P. E. M. Siegbahn and M. R. A. Blomberg, *Chem. Phys.*, 1982, **66**, 197–207.

60 K. Andersson, P. A. Malmqvist, B. O. Roos, A. J. Sadlej and K. Wolinski, *J. Phys. Chem.*, 1990, **94**, 5483–5488.

61 K. Andersson, P.-A. k Malmqvist and B. O. Roos, *J. Chem. Phys.*, 1992, **96**, 1218–1226.

62 J. Finley, P.-A. k Malmqvist, B. O. Roos and L. Serrano-Andrés, *Chem. Phys. Lett.*, 1998, **288**, 299–306.

63 A. A. Granovsky, *J. Chem. Phys.*, 2011, **134**, 214113.

64 T. Shiozaki, W. Györffy, P. Celani and H.-J. Werner, *J. Chem. Phys.*, 2011, **135**, 081106.

65 I. Fdez. Galván, M. Vacher, A. Alavi, C. Angeli, F. Aquilante, J. Autschbach, J. J. Bao, S. I. Bokarev, N. A. Bogdanov, R. K. Carlson, L. F. Chibotaru, J. Creutzberg, N. Dattani, M. G. Delcey, S. S. Dong, A. Dreuw, L. Freitag, L. M. Frutos, L. Gagliardi, F. Gendron, A. Giussani, L. González, G. Grell, M. Guo, C. E. Hoyer, M. Johansson, S. Keller, S. Knecht, G. Kovačević, E. Källman, G. Li Manni, M. Lundberg, Y. Ma, S. Mai, J. A. P. Malhado, P. A. K. Malmqvist, P. Marquetand, S. A. Mewes, J. Norell, M. Olivucci, M. Oppel, Q. M. Phung, K. Pierloot, F. Plasser, M. Reiher, A. M. Sand, I. Schapiro, P. Sharma, C. J. Stein, L. K. Sørensen, D. G. Truhlar, M. Ugandi, L. Ungur, A. Valentini, S. Vancoillie, V. Veryazov, O. Weser, T. A. Wesołowski, P.-O. Widmark, S. Wouters, A. Zech, J. P. Zobel and R. Lindh, *J. Chem. Theory Comput.*, 2019, **15**, 5925–5964.

66 F. Aquilante, J. Autschbach, A. Baiardi, S. Battaglia, V. A. Borin, L. F. Chibotaru, I. Conti, L. De Vico, M. Delcey, I. F. Galván, N. Ferré, L. Freitag, M. Garavelli, X. Gong, S. Knecht, E. D. Larsson, R. Lindh, M. Lundberg, P. A. K. Malmqvist, A. Nenov, J. Norell, M. Odelius, M. Olivucci, T. B. Pedersen, L. Pedraza-González, Q. M. Phung, K. Pierloot, M. Reiher, I. Schapiro, J. Segarra-Martí, F. Segatta, L. Seijo, S. Sen, D.-C. Sergentu, C. J. Stein, L. Ungur, M. Vacher, A. Valentini and V. Veryazov, *J. Chem. Phys.*, 2020, **152**, 214117.

67 P.-O. Widmark, P.-A. k Malmqvist and B. O. Roos, *Theoret. Chim. Acta*, 1990, **77**, 291–306.

68 B. O. Roos, R. Lindh, P.-A. K. Malmqvist, V. Veryazov and P.-O. Widmark, *J. Phys. Chem. A*, 2004, **108**, 2851–2858.

69 B. O. Roos, V. Veryazov and P.-O. Widmark, *Theor. Chem. Acc.*, 2004, **111**, 345–351.

70 J. Chmeliov, W. P. Bricker, C. Lo, E. Jouin, L. Valkunas, A. V. Ruban and C. D. P. Duffy, *Phys. Chem. Chem. Phys.*, 2015, **17**, 15857–15867.

71 K. Falahati, C. Hamerla, M. Huix-Rotllant and I. Burghardt, *Phys. Chem. Chem. Phys.*, 2018, **20**, 12483–12492.

72 V. V. Poddubnyy, M. I. Kozlov and I. O. Glebov, *Chem. Phys. Lett.*, 2021, **778**, 138792.

73 G. Ghigo, B. O. Roos and P.-A. K. Malmqvist, *Chem. Phys. Lett.*, 2004, **396**, 142–149.

74 N. Forsberg and P.-A. K. Malmqvist, *Chem. Phys. Lett.*, 1997, **274**, 196–204.

75 H. Tal-Ezer and R. Kosloff, *J. Chem. Phys.*, 1984, **81**, 3967–3971.

76 R. Franke, *Comput. Math. with Appl.*, 1982, **8**, 273–281.

77 E. B. Wilson, J. C. Decius and P. C. Cross, *Molecular Vibrations: The Theory of Infrared and Raman Vibrational Spectra*, Dover Publications, 1980.

78 L. J. Schaad and J. Hu, *J. Mol. Struct. THEOCHEM*, 1989, **185**, 203–215.

79 J. Stare and G. G. Balint-Kurti, *J. Phys. Chem. A*, 2003, **107**, 7204–7214.

80 M. Kowalewski, J. Mikosch, R. Wester and R. de Vivie-Riedle, *J. Phys. Chem. A*, 2014, **118**, 4661–4669.

81 R. Kosloff and H. Tal-Ezer, *Chem. Phys. Lett.*, 1986, **127**, 223–230.

82 M. Taniguchi, H. Du and J. S. Lindsey, *Photochem. Photobiol.*, 2018, **94**, 277–289.

83 M. Taniguchi and J. S. Lindsey, *Photochem. Photobiol.*, 2018, **94**, 290–327.

84 A. B. J. Parusel and S. Grimme, *J. Phys. Chem. B*, 2000, **104**, 5395–5398.
85 D. Zigmantas, R. G. Hiller, V. Sundström and T. Polívka, *Proc. Natl. Acad. Sci. U. S. A.*, 2002, **99**, 16760–16765.
86 M. K. Roos, S. Reiter and R. de Vivie-Riedle, *Chem. Phys.*, 2018, **515**, 586–595.
87 J. D. Coe and T. J. Martínez, *J. Phys. Chem. A*, 2006, **110**, 618–630.
88 P. Chakraborty, Y. Liu, T. Weinacht and S. Matsika, *J. Chem. Phys.*, 2020, **152**, 174302.
89 C. Camacho, R. Cimiraglia and H. A. Witek, *Phys. Chem. Chem. Phys.*, 2010, **12**, 5058–5060.
90 N. Ben Amor, A. Soupart and M.-C. Heitz, *J. Mol. Model.*, 2017, **23**, 53.
91 J. P. Zobel, J. J. Nogueira and L. González, *Chem. Sci.*, 2017, **8**, 1482–1499.
92 G. Giuliani, F. Melaccio, S. Gozem, A. Cappelli and M. Olivucci, *J. Chem. Theory Comput.*, 2021, **17**, 605–613.
93 A. Kerridge, *Phys. Chem. Chem. Phys.*, 2013, **15**, 2197–2209.